International Journal of Computational Methods
Vol. 2, No. 4 (2005) 645–665

World Scientific
www.worldscientific.com

A LINEARLY CONFORMING POINT INTERPOLATION METHOD (LC-PIM) FOR 2D SOLID MECHANICS PROBLEMS

G. R. LIU, G. Y. ZHANG* and K. Y. DAI
Centre for Advanced Computations in Engineering Science (ACES)
Department of Mechanical Engineering
National University of Singapore
10 Kent Ridge Crescent, Singapore, 119260
**g0203729@nus.edu.sg*

Y. Y. WANG
Institute of High Performance Computing, Singapore

Z. H. ZHONG, G. Y. LI and X. HAN
Key Laboratory of Advanced Technology for Vehicle
Body Design & Manufacture, M.O.E
Hunan University, Changsha, 410082, P. R. China

Received 25 June 2005
Revised 12 November 2005
Accepted 2 December 2005

A linearly conforming point interpolation method (LC-PIM) is developed for 2D solid problems. In this method, shape functions are generated using the polynomial basis functions and a scheme for the selection of local supporting nodes based on background cells is suggested, which can always ensure the moment matrix is invertible as long as there are no coincide nodes. Galerkin weak form is adopted for creating discretized system equations, and a nodal integration scheme with strain smoothing operation is used to perform the numerical integration. The present LC-PIM can guarantee linear exactness and monotonic convergence for the numerical results. Numerical examples are used to examine the present method in terms of accuracy, convergence, and efficiency. Compared with the finite element method (FEM) using linear triangle elements and the radial point interpolation method (RPIM) using Gauss integration, the LC-PIM can achieve higher convergence rate and better efficiency.

Keywords: Meshfree; linearly conforming; point interpolation method; nodal integration.

1. Introduction

The development of meshfree methods have achieved remarkable progress in recent years. Methods and techniques developed so far include the general finite difference

*Corresponding author.

method [Liszka and Orkisz, 1980], the smooth particle hydrodynamic (SPH) method [Lucy, 1977; Liu and Liu, 2003], the diffuse element method (DEM) [Nayroles *et al.*, 1992], the element-free Galerkin (EFG) method [Belytschko *et al.*, 1994], reproducing kernel particle method (RKPM) (Liu *et al.*, 1995), and the meshless local Petrov-Galerkin (MLPG) method [Atluri and Zhu, 1998], etc.

The point interpolation method is a meshfree method constructed using Galerkin weak form and shape functions that are contributed based on a small set of nodes distributed in a local support domain using simple interpolation [Liu, 2002]. Two types of PIM shape functions have been used with different forms of basis functions, i.e., polynomial basis functions [Liu and Gu, 2001a; Liu, 2002] and radial basis functions [Wang and Liu, 2002a; Liu and Gu, 2001b]. PIM using polynomial basis functions is termed as polynomial PIM. In the original polynomial PIM, the problem of singular moment matrix can occur, resulting in termination of the computation. To overcome the singularity problem, RBFs augmented with polynomial terms are used to generate shape functions and the method so constructed is termed as RPIM. RPIM can effectively solve the problem of singularity and has been extended for solving many types of problems [Wang *et al.*, 2002; Dai *et al.*, 2005; Liu *et al.*, 2005; etc.]. However, the original PIM and RPIM using Gauss integration cannot guarantee a linear exactness in the solutions due to the inconformability or incompatibility. This work presents a linearly conforming PIM or LC-PIM based on nodal integration technique [Chen *et al.*, 2001]. The present LC-PIM possesses the following novel features: (1) A simple scheme for local supporting node selection is suggested based on triangular background cells, which overcomes the singular moment matrix issue, and ensures the efficiency in computing PIM shape functions; (2) Shape functions generated using polynomial basis functions and simple interpolation ensure that the PIM shape functions possesses at least linearly consistency and the Delta function property, which facilitates easy implementation of essential boundary conditions; (3) The use of nodal integration scheme with strain smoothing operation converts the domain integration required in the weak form to line integrations on the boundary of the smoothing cells, which ensures the conformability of the displacement. Due to these novel features, the present LC-PIM is easy to implement, guarantees monotonic convergence, and is computationally efficient.

2. Formulation

This section presents detailed formulations for the linearly conforming point interpolation method (LC-PIM).

2.1. *Point interpolation*

Polynomials have been used as basis functions in the interpolation to create shape functions in many numerical methods, such as the FEM. In the FEM, however, the interpolation is based on elements that are perfectly (no gap and overlapping) connected. In the present LC-PIM, our interpolation is based on a small set of nodes

(typically three or six nodes are used in the work) in a local support domain that can overlap with other support domains.

Consider a continuous function $u(\mathbf{x})$, which is displacement for our solid mechanics problems. It can be approximated in the vicinity of $\mathbf{x}$ as follows.

$$u(\mathbf{x}) = \sum_{i=1}^{n} p_i(\mathbf{x})\, a_i = \mathbf{p}^{\mathrm{T}}(\mathbf{x})\, \mathbf{a}, \tag{1}$$

where $p_i(\mathbf{x})$ is polynomial basis function of $\mathbf{x} = [x, y]^{\mathrm{T}}$, n is the number of polynomial terms, and a_i is the corresponding coefficient yet to be determined. The polynomial basis $p_i(\mathbf{x})$ is usually built utilizing the Pascal's triangles, and a complete basis is preferred because of the requirement of consistency. The complete polynomial basis of orders 1 and 2 can be written in the following forms.

$$\begin{array}{ll} \mathbf{p}^{\mathrm{T}}(\mathbf{x}) = \{1 \quad x \quad y\} & \text{Basis of compelte 1st order.} \\ \mathbf{p}^{\mathrm{T}}(\mathbf{x}) = \{1 \quad x \quad y \quad x^2 \quad xy \quad y^2\} & \text{Basis of compelte 2nd order.} \end{array} \tag{2}$$

In the original PIM [Liu, 2002], a local support domain containing of n field nodes is formed for the point of interest $\mathbf{x}$. The coefficients a_i in Eq. (1) can then be determined by enforcing $u(\mathbf{x})$ to be the nodal displacements at these n nodes. Leading to n equations:

$$\begin{cases} u(x_1, y_1) = a_1 + a_2 x_1 + a_3 y_1 + \cdots + a_n p_n(\mathbf{x}_1) \\ u(x_2, y_2) = a_1 + a_2 x_2 + a_3 y_2 + \cdots + a_n p_n(\mathbf{x}_2) \\ \qquad\qquad \vdots \\ u(x_n, y_n) = a_1 + a_2 x_n + a_3 y_n + \cdots + a_n p_n(\mathbf{x}_n) \end{cases} \tag{3}$$

In the matrix form, it can be written as

$$\mathbf{U}_s = \mathbf{P}_n \mathbf{a}, \tag{4}$$

where $\mathbf{U}_s$ is the vector of nodal displacements,

$$\mathbf{U}_s = \{u_1 \quad u_2 \quad u_3 \quad \cdots \quad u_n\}^{\mathrm{T}}, \tag{5}$$

$\mathbf{a}$ is the vector of unknown coefficients,

$$\mathbf{a} = \{a_1 \quad a_2 \quad a_3 \quad \cdots \quad a_n\}^{\mathrm{T}}, \tag{6}$$

$\mathbf{P}_n$ is the polynomial moment matrix.

$$\mathbf{P}_n = \begin{bmatrix} 1 & x_1 & y_1 & x_1 y_1 & \cdots & p_n(\mathbf{x}_1) \\ 1 & x_2 & y_2 & x_2 y_2 & \cdots & p_n(\mathbf{x}_2) \\ 1 & x_3 & y_3 & x_3 y_3 & \cdots & p_n(\mathbf{x}_3) \\ \vdots & \vdots & \vdots & \vdots & \ddots & \vdots \\ 1 & x_n & y_n & x_n y_n & \cdots & p_n(\mathbf{x}_n) \end{bmatrix}. \tag{7}$$

Assuming the existence of $\mathbf{P}_n^{-1}$, a unique solution for $\mathbf{a}$ can be obtained as

$$\mathbf{a} = \mathbf{P}_n^{-1} \mathbf{U}_s. \tag{8}$$

Substituting Eq. (8) back into Eq. (1) yields

$$u(\mathbf{x}) = \mathbf{P}^{\mathrm{T}}(\mathbf{x})\mathbf{P}_n^{-1}\mathbf{U}_s = \sum_{i=1}^{n} \varphi_i u_i = \mathbf{\Phi}^{\mathrm{T}}(\mathbf{x})\mathbf{U}_s, \tag{9}$$

where $\mathbf{\Phi}(\mathbf{x})$ is the vector of PIM shape functions:

$$\mathbf{\Phi}^{\mathrm{T}}(\mathbf{x}) = \{\varphi_1(\mathbf{x}) \quad \varphi_2(\mathbf{x}) \quad \cdots \quad \varphi_n(\mathbf{x})\}. \tag{10}$$

The kth derivatives of the shape functions can be easily obtained, but they are not required in our LC-PIM formulation due to the use of strain smoothing operation described in the following.

2.2. *Node selection*

Note that the previous formulations are obtained based on the assumption that the moment matrix $\mathbf{P}_n$ is invertible. However, this condition cannot always be met. It depends on the locations of the node in the local support domain and the terms of monomials used in the basis functions (see, e.g., Liu [2002]). Some techniques have been suggested to overcome the singularity problem of moment matrix, such as the use of matrix triangularization algorithm [Liu and Gu, 2003] and the use of radial basis functions augmented with the polynomial basis [Wang and Liu, 2002a].

We note the fact that in meshfree methods based on weak forms, background cells have to be used to performing the numerical integration. Triangular cells are preferred due to (1) the adaptiveness of the triangular cells to complex geometry, and (2) triangular cells can be created automatically and updated easily for adaptive analyses [Liu, 2002]. Since the background cells are available, it is natural to make use them for other purposes, such as node selection. In this work, a simple scheme for local supporting node selection is suggested based on the background triangular cells for shape function construction as shown in Fig. 1. The background triangular cells are classified into two groups: interior cells and edge cells. An interior cell is a cell that has no edge on the boundary of the problem domain, and an edge cell is a cell that has at least one edge on the boundary of the problem domain. When the point of interest is located in an interior cell such as cell i, we use six nodes for interpolation: three nodes located at the vertices of this cell, and the other three nodes located at the remote vertices of the three neighboring cells. These six nodes are labeled as i_1–i_6 in Fig. 2. When the point of interest $\mathbf{x}$ is located in an edge cell, for example cell j, we simply use only three nodes that are located at the vertices for the interpolation of cell j labeled as j_1–j_3 in Fig. 2. This simple means of node selection has the following features.

1) It can be easily proven (by simple inspection) that the moment matrix will never be singular, unless there are duplicated nodes in the problem domain.
2) At any point in an interior cell, the PIM shape functions has 2nd order consistency.
3) At any point in an edge cell the PIM shape functions has linear consistency. This allows easy imposition of essential boundary conditions.

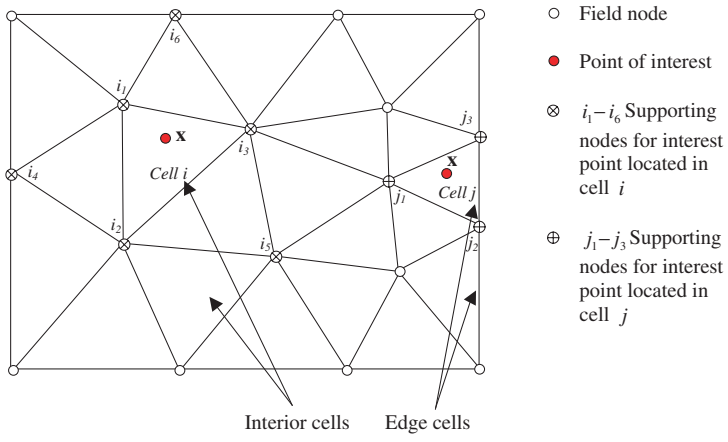

Fig. 1. Illustration of background cells of triangles and the selection of supporting nodes.

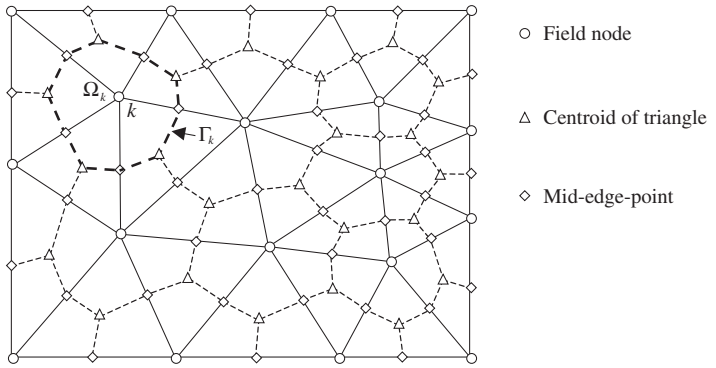

Fig. 2. Illustration of background triangular cells and the smoothing cells created by sequentially connecting the centroids with the mid-edge-points of the surrounding triangles of a node.

4) Conformability (or compatibility) can be ensured by the later implementation of nodal integrations with smoothing operation on strains.

Note that the easiest and also workable way of node selection is to use three nodes that are the vertices of the triangular cells that contain the point of interest **x**. This simple node selection leads to similar but not necessarily the same results (depending on how the strain smoothing is performed) as that of the linear triangular FEM. This has been confirmed in our intensive studying numerical examples.

2.3. *Nodal integration of weak form*

2.3.1. *Galerkin weak form and nodal integration*

Consider a 2D solid mechanics problem defined in domain Ω bounded by Γ $(= \Gamma_u + \Gamma_t)$, this problem can be expressed by the following equations [Timoshenko and Goodier, 1970].

Equilibrium equation:

$$\mathbf{L}^{\mathrm{T}}\boldsymbol{\sigma} + \mathbf{b} = 0 \quad \text{in } \Omega, \tag{11}$$

where $\mathbf{L}^{\mathrm{T}} = \begin{bmatrix} \frac{\partial}{\partial x} & 0 & \frac{\partial}{\partial y} \\ 0 & \frac{\partial}{\partial y} & \frac{\partial}{\partial x} \end{bmatrix}$ is a differential operator; $\boldsymbol{\sigma}^{\mathrm{T}} = \{\sigma_{xx} \quad \sigma_{yy} \quad \tau_{xy}\}$ is the stress vector, $\mathbf{u}^{\mathrm{T}} = \{u \quad v\}$ is the displacement vector, $\mathbf{b}^{\mathrm{T}} = \{b_x \quad b_y\}$ is the body force vector.

Essential boundary conditions:

$$\mathbf{u} = \bar{\mathbf{u}} \quad \text{on } \Gamma_u, \tag{12}$$

where $\bar{\mathbf{u}}$ is the prescribed displacement on the essential boundaries.

Natural boundary conditions:

$$\boldsymbol{\sigma} \cdot \mathbf{n} = \bar{\mathbf{t}} \quad \text{on } \Gamma_t, \tag{13}$$

where $\bar{\mathbf{t}}$ is the prescribed traction on the natural boundaries, and vector $\mathbf{n}$ is the unit outward normal.

The standard Galerkin weak form for this problem can be expressed as

$$\int_\Omega (\mathbf{L}\delta\,\mathbf{u})^{\mathrm{T}}(\mathbf{D}\mathbf{L}\mathbf{u})d\Omega - \int_\Omega \delta\,\mathbf{u}^{\mathrm{T}}\mathbf{b}d\Omega - \int_{\Gamma_t} \delta\,\mathbf{u}^{\mathrm{T}}\bar{\mathbf{t}}d\Gamma = 0, \tag{14}$$

where $\mathbf{D}$ is the matrix of material constants.

Substituting Eq. (9) into Eq. (14), the discretized system equation can be in the following matrix form.

$$\mathbf{K}\mathbf{u} = \mathbf{f}, \tag{15}$$

where

$$\mathbf{K}_{ij} = \int_\Omega \mathbf{B}_i^{\mathrm{T}}\mathbf{D}\mathbf{B}_j d\Omega, \tag{16}$$

$$\mathbf{f}_i = \int_{\Gamma_t} \varphi_i \bar{\mathbf{t}} d\Gamma + \int_\Omega \varphi_i \mathbf{b} d\Omega, \tag{17}$$

$$\mathbf{B}_i = \begin{bmatrix} \varphi_{i,x} & 0 \\ 0 & \varphi_{i,y} \\ \varphi_{i,y} & \varphi_{i,x} \end{bmatrix}. \tag{18}$$

In carrying out the numerical domain integration in Eqs. (16) and (17), the nodal integration scheme [Chen *et al.*, 2001] is adopted to perform the numerical integration. The problem domain Ω is divided into smoothing domains Ω_k centered by node k, as shown in Fig. 2. The sub-domain Ω_k is constructed using background triangular cells by connecting sequentially the mid-edge-point to the centroids of the triangles. The boundary of Ω_k is labeled as Γ_k (shown in Fig. 2) and the union of all Ω_k forms Ω exactly. We then have

$$\mathbf{K}_{ij} = \sum_{k=1}^{N} \mathbf{K}_{ij}^{(k)}, \tag{19}$$

where

$$\mathbf{K}_{ij}^{(k)} = \int_{\Omega_k} \mathbf{B}_i^{\mathrm{T}} \mathbf{D} \mathbf{B}_j d\Omega. \tag{20}$$

2.3.2. *Smoothing strain operation*

Note that the PIM shape functions obtained in Secs. 2.1 and 2.2 have at least linear consistency. To guarantee a linear exactness in the solution based on the Galerkin weak form, a smoothing operation is performed on the strains [Chen *et al.*, 2001].

$$\tilde{\varepsilon}_{ij}^h(\mathbf{x}_k) = \int_{\Omega_k} \tilde{\varepsilon}_{ij}^h(\mathbf{x}) \Psi(\mathbf{x} - \mathbf{x}_k) d\Omega, \tag{21}$$

where Ψ is a smoothing function.

For simplicity, we use

$$\Psi(\mathbf{x} - \mathbf{x}_k) = \begin{cases} 1/A_k & \mathbf{x} \in \Omega_k \\ 0 & \mathbf{x} \notin \Omega_k \end{cases}, \tag{22}$$

where $A_k = \int_{\Omega_k} d\Omega$ is the area of smoothing domain for node k.

Substituting Eq. (22) into Eq. (21) and integrating by parts, we obtain

$$\begin{aligned} \tilde{\varepsilon}_{ij}^h(\mathbf{x}_k) &= \frac{1}{A_k} \int_{\Omega_k} \tilde{\varepsilon}_{ij}^h(\mathbf{x}) d\Omega \\ &= \frac{1}{A_k} \int_{\Omega_k} \frac{1}{2} \left(\frac{\partial u_i^h}{\partial x_j} + \frac{\partial u_j^h}{\partial x_i} \right) d\Omega \\ &= \frac{1}{2A_k} \int_{\Gamma_k} (u_i^h n_j + u_j^h n_i) d\Gamma, \end{aligned} \tag{23}$$

where Γ_k is the boundary of the smoothing domain for node k. Using the PIM shape functions in Eq. (23), the smoothed strain can be written in the following matrix form.

$$\tilde{\boldsymbol{\varepsilon}}^h(\mathbf{x}_k) = \sum_{i \in G_k} \tilde{\mathbf{B}}_i(\mathbf{x}_k) \mathbf{U}_i, \tag{24}$$

where G_k contains a number of nodes in the influence domain of node k or those nodes whose shape function support cover node k. In two dimensional space,

$$\tilde{\boldsymbol{\varepsilon}}^{h^{\mathrm{T}}} = \{\tilde{\boldsymbol{\varepsilon}}_{11}^h \quad \tilde{\varepsilon}_{22}^h \quad \tilde{\varepsilon}_{12}^h\}, \quad \mathbf{U}_i^{\mathrm{T}} = \{u_{1i} \quad u_{2i}\}, \tag{25}$$

$$\tilde{\mathbf{B}}_i(\mathbf{x}_k) = \begin{bmatrix} \tilde{b}_{i1}(\mathbf{x}_k) & 0 \\ 0 & \tilde{b}_{i2}(\mathbf{x}_k) \\ \tilde{b}_{i2}(\mathbf{x}_k) & \tilde{b}_{i1}(\mathbf{x}_k) \end{bmatrix}, \tag{26}$$

$$\tilde{b}_{il} = \frac{1}{A_k} \int_{\Gamma_k} \varphi_i(\mathbf{x}) n_l(\mathbf{x}) d\Gamma \quad (l = 1, 2), \tag{27}$$

Applying Gauss integration along each segment of boundary Γ_k of smoothing domain Ω_k, the above equation can be written in algebraic form as

$$\tilde{b}_{il} = \frac{1}{A_k} \sum_{m=1}^{N_s} \left[\sum_{n=1}^{N_g} w_n(\varphi_i(\mathbf{x}_{mn}) n_i(\mathbf{x}_m)) \right], \tag{28}$$

where N_s is the number of segments of the boundary Γ_k, N_g is the number of Gauss points distributed in each segment, and w_n is the corresponding weight number of Gauss integration scheme. In the present method, $n_g = 2$ is used.

Then Eq. (20) can be written as,

$$\mathbf{K}_{ij}^{(k)} = \int_{\Omega_k} \tilde{\mathbf{B}}_i^{\mathrm{T}} \mathbf{D} \tilde{\mathbf{B}}_j d\Omega \,. \tag{29}$$

It is proven that the use of Eq. (29) in place of Eq. (20) can exactly satisfy the so-called integration constraint, which is the requirement of obtaining linear exactness in the solutions based on the Galerkin weak form [Chen *et al.*, 2001].

3. Numerical Examples

Several numerical examples are studied in this section. The materials used are all linear elastic with Young's modulus $E = 3.0 \times 10^7$ and Poisson's ratio $\nu = 0.3$. The units used in this paper can be any consistent unit based on international standard unit system. The error indicators in displacement and energy are respectively defined as follows,

$$e_d = \sqrt{\frac{\sum_{i=1}^{n} (u_i^{\text{exact}} - u_i^{\text{numerical}})^2}{\sum_{i=1}^{n} (u_i^{\text{exact}})^2}}, \tag{30}$$

$$e_e = \frac{1}{A} \sqrt{\frac{1}{2} \int_{\Omega} (\boldsymbol{\varepsilon}^{\text{exact}} - \boldsymbol{\varepsilon}^{\text{numerical}})^{\mathrm{T}} \, \mathbf{D} (\boldsymbol{\varepsilon}^{\text{exact}} - \boldsymbol{\varepsilon}^{\text{numerical}}) d\Omega}, \tag{31}$$

where the superscript *exact* notes the exact or analytical solution, *numerical* notes a numerical solution obtained using a numerical method including the present LC-PIM, and A is the area of the problem domain.

3.1. *Standard patch test*

For a numerical method working for solid mechanics problems, the sufficient requirement for convergence is to pass the standard patch test [Zienkiewicz and Taylor, 2000]. Therefore, the first example is the standard patch test using the present LC-PIM. The problem is studied in a 10×10 square domain, and the displacements are prescribed on all outside boundaries by the following linear function.

$$\begin{cases} u_x = 0.6x \\ u_y = 0.6y \end{cases}. \tag{32}$$

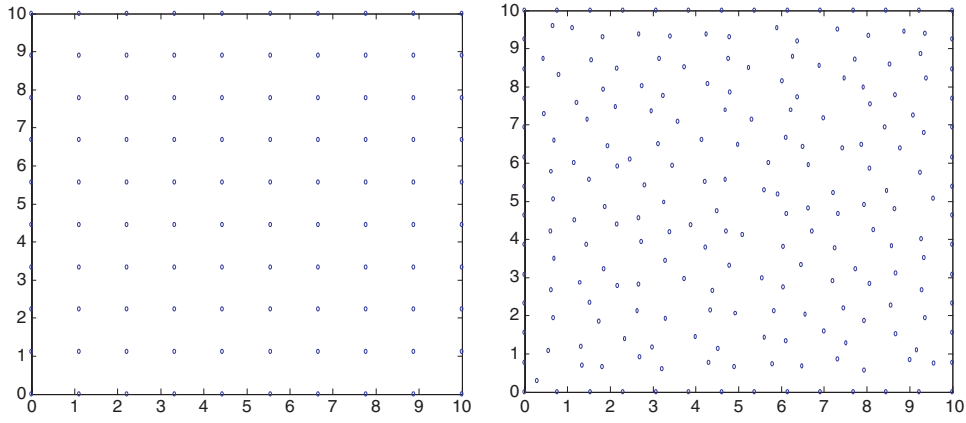

(a) 100 regularly distributed nodes. (b) 109 irregularly distributed nodes.

Fig. 3. Node distributions for the standard patch test.

The patch is represented using regular and irregular nodes shown in Fig. 3. The errors in displacement defined in Eq. (30) are found to be 2.35×10^{-14} for the patch of regular nodes and 4.77×10^{-14} for the patch of irregular nodes. This example demonstrates that, numerically the present LC-PIM will monotonically converge due to its ability to reproduce linear fields and the use of the Galerkin weak form.

3.2. *Cantilever beam*

A benchmark problem of cantilever beam with length L and height D is studied. The beam is subjected to a parabolic traction on the right edge of the beam, as shown in Fig. 4. As the beam is assumed to have unit thickness, analytical solution based on the plane stress theory is available as follows [Timoshenko and Goodier, 1970],

$$u_x = -\frac{py}{6EI}\left[(6L - 3x)x + (2 + v)\left(y^2 - \frac{D^2}{4}\right)\right], \tag{33}$$

$$u_y = \frac{p}{6EI}\left[3vy^2(L - x) + (4 + 5v)\frac{D^2 x}{4} + (3L - x)x^2\right], \tag{34}$$

$$\sigma_x = -\frac{p(L - x)y}{I}, \tag{35}$$

$$\sigma_y = 0, \tag{36}$$

$$\sigma_{xy} = \frac{p}{2I}\left[\frac{D^2}{4} - y^2\right], \tag{37}$$

where I is the moment of the inertia given as $I = D^3/12$.

The values of the parameters are taken as: $L = 50, D = 10$ and $P = -1000$.

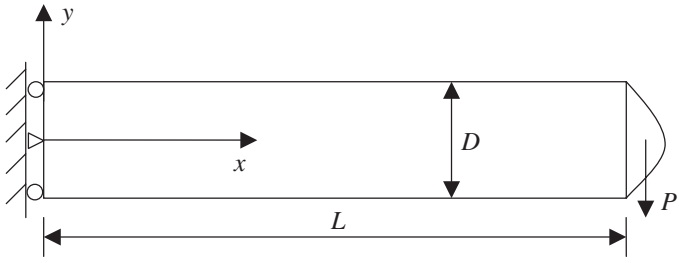

Fig. 4. Cantilever beam subjected to a parabolic traction on the right edge.

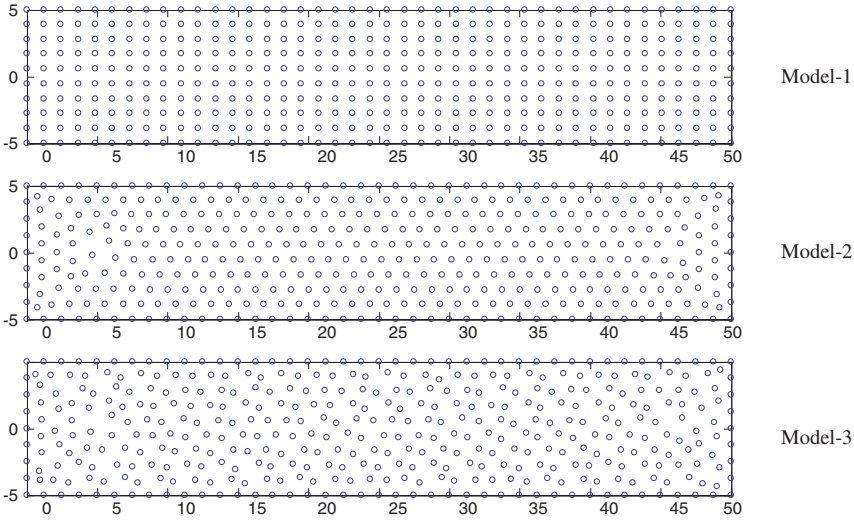

Fig. 5. Three models of nodal distributions for the cantilever beam.

3.2.1. *Effects of the irregularity in the nodal distribution*

To investigate the effect of the irregularities in nodal distribution, three models of 420 distributed nodes with different status of irregularity (shown in Fig. 5) are used to examine the present method. The results of deflection along the neutral line and the shear stress along the line ($x = L/2$) of the beam are plotted together with the analytical solutions in Fig. 6. It can be found that the numerical results of these three models obtained using the present LC-PIM are all in good agreement with the analytical ones, and the irregularity of the nodal distribution has little effect on the numerical results.

3.2.2. *Convergence and efficiency of the LC-PIM*

To investigate the properties of convergence and efficiency of the present method, four models with 94, 181, 399, and 801 irregularly distributed nodes are employed.

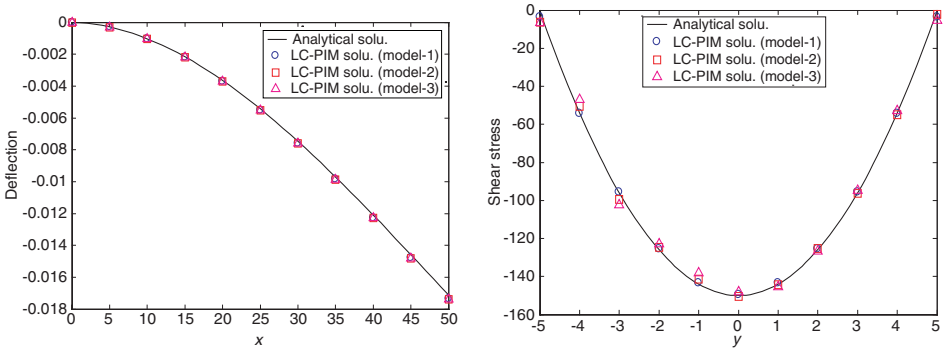

(a) Deflection distribution along the neutral line.

(b) Shear stress distribution along the line $x = L/2$.

Fig. 6. Numerical results obtained using the LC-PIM and three models of node distributions.

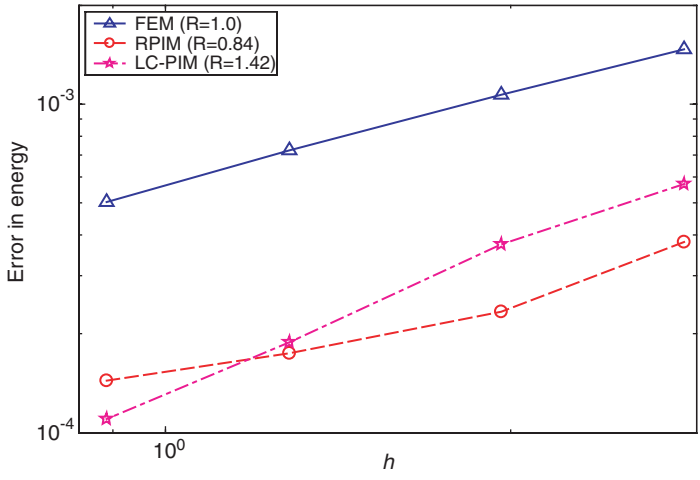

Fig. 7. Comparison of convergence rate between FEM, RPIM, and LC-PIM.

For comparison, three methods, FEM, RPIM, and LC-PIM, are all used for this problem. In FEM, linear element of 3-node triangle is employed. In the RPIM, MQ-RBFs augmented with linear polynomials are adopted with parameters $q = 1.03$, $\alpha_c = 4.0$, and $\alpha_s = 2.0$ for circular local support domain. These values of parameters have been found to perform well for most problems [Wang and Liu, 2002b; Liu, 2002; Liu *et al.*, 2005]. The results of error in energy norm against h are plotted in Fig. 7, where h is the averaged element size in the FEM. Compared with linear FEM, the LC-PIM not only achieves a higher convergence rate but also obtains more accurate results. This is due to the use of more nodes in creating the shape functions, which is made possible in the meshfree context, thus allowing the use of nodes beyond the elements for shape function construction. Compared with

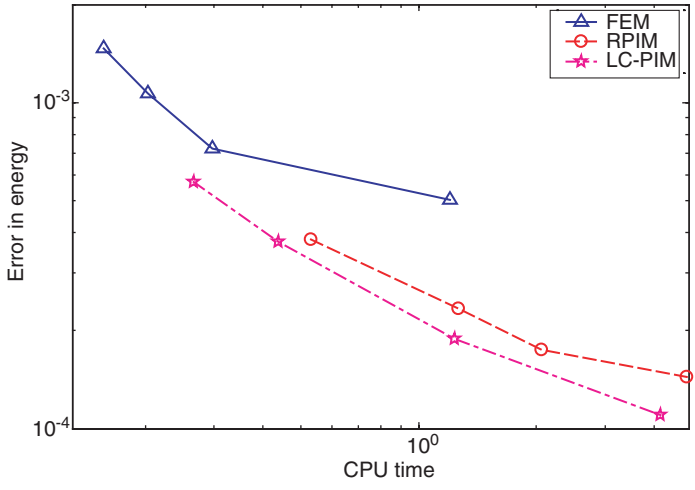

Fig. 8. Comparison of efficiency between FEM, RPIM, and LC-PIM.

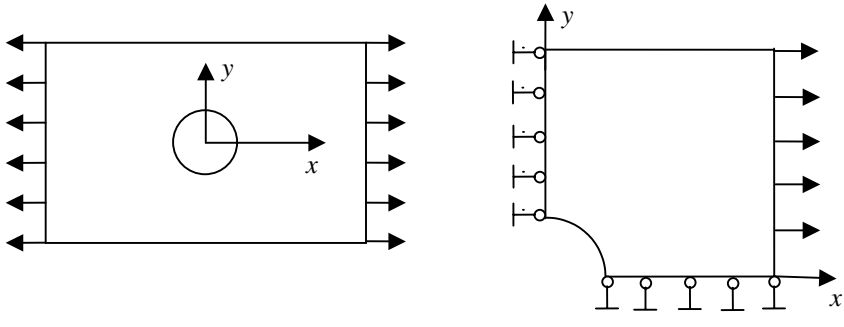

Fig. 9. Infinite plate with a circular hole subjected to a tensile force and its quarter model.

the RPIM, the LC-PIM obtains a much higher convergence rate and comparable accuracy. In Fig. 8, the energy errors obtained using these three methods are plotted against the CPU time, which shows the efficiency of the methods. The results show that the present method is more efficient than both the linear FEM and the RPIM using exactly the same set of nodes to discretize the problem domain.

3.3. *Infinite plate with a circular hole*

An infinite plate with a central circular hole ($a = 10$) subjected to a unidirectional tensile ($T_x = 10$) is studied. Due to its two-fold symmetry, only one quarter shown in Fig. 9 is modeled. Symmetry conditions are imposed on the left and bottom edges, and the inner boundary of the hole is traction free. For this benchmark problem,

the analytical solution is available [Timoshenko and Goodier, 1970]:

$$u_r = \frac{T_x}{4\mu}\left\{r\left[\frac{(\kappa-1)}{2}+\cos(2\theta)\right]+\frac{a^2}{r}[1+(1+\kappa)\cos(2\theta)]-\frac{a^4}{r^3}\cos(2\theta)\right\}, \tag{38}$$

$$u_\theta = \frac{T_x}{4\mu}\left[(1-\kappa)\frac{a^2}{r}-r-\frac{a^4}{r^3}\right]\sin(2\theta), \tag{39}$$

$$\sigma_{xx} = T_x\left\{1-\frac{a^2}{r^2}\left[\frac{3}{2}\cos(2\theta)+\cos(4\theta)\right]+\frac{3a^4}{2r^4}\cos(4\theta)\right\}, \tag{40}$$

$$\sigma_{yy} = -T_x\left\{\frac{a^2}{r^2}\left[\frac{1}{2}\cos(2\theta)-\cos(4\theta)\right]+\frac{3a^4}{2r^4}\cos(4\theta)\right\}, \tag{41}$$

$$\sigma_{xy} = -T_x\left\{\frac{a^2}{r^2}\left[\frac{1}{2}\sin(2\theta)+\sin(4\theta)\right]-\frac{3a^4}{2r^4}\sin(4\theta)\right\}, \tag{42}$$

where

$$\mu = \frac{E}{2(1+v)}, \quad \kappa = \begin{cases} 3-4v & \text{Plane strain} \\ \dfrac{3-v}{1+v} & \text{Plane stress} \end{cases} \tag{43}$$

In this study, plane stress problem is considered and the domain is discretized using 411 irregularly distributed nodes. The computed displacements for nodes located along the left and the bottom edge are calculated and plotted in Fig. 10. Figure 11 shows the distribution of normal stress along the left edge. These figures show again that all the numerical results agree well with the analytical ones.

3.4. *Internal pressurized hollow cylinder*

A thick-walled hollow cylinder subjected to internal pressure is analyzed as another benchmark problem in this section. As shown in Fig. 12, the cylinder is of internal radius $a = 10$, outer radius $b = 25$, and the internal pressure $p = 100$ units. The

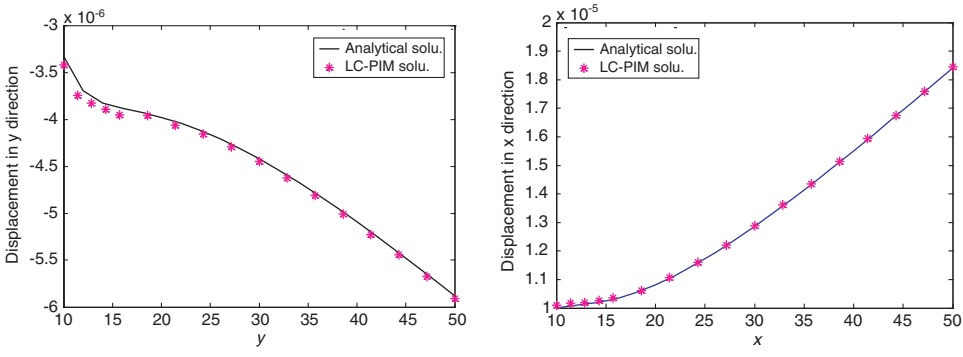

(a) Distribution of U_y along the left edge. (b) Distribution of U_x along the bottom edge.

Fig. 10. Displacement distribution along the boundary edges for the problem of a plate with a circular hole.

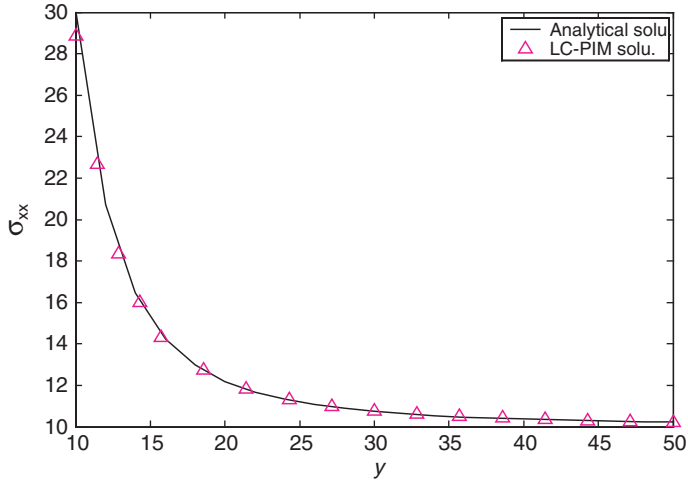

Fig. 11. Stress distribution along the left edge for the problem of a plate with a circular hole.

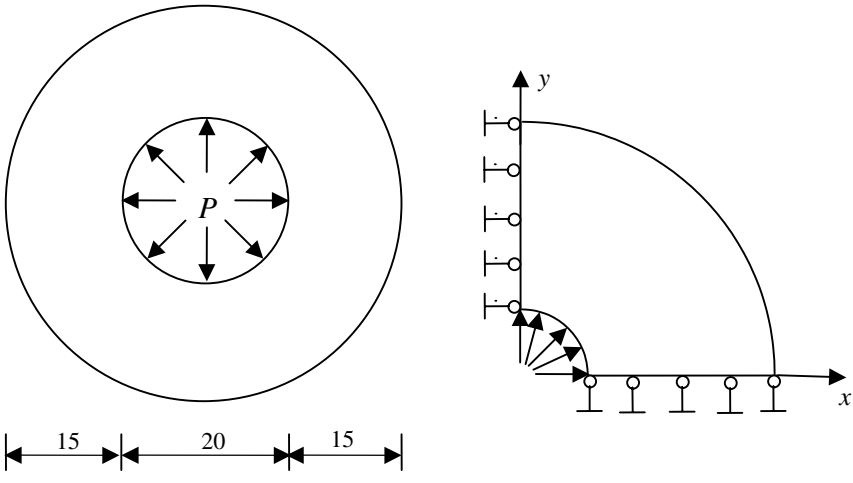

Fig. 12. Hollow cylinder subjected to internal pressure and its quarter model.

thickness of the cylinder is of one unit and the analytical solution is available for this plane stress problem [Timoshenko and Goodier, 1970].

$$u_r = \frac{pa^2}{E(b^2 - a^2)\, r}[(1 - v)\, r^2 + (1 + v)\, b^2], \tag{44}$$

$$\sigma_r = \frac{a^2 p}{b^2 - a^2}\left(1 - \frac{b^2}{r^2}\right), \tag{45}$$

$$\sigma_\theta = \frac{a^2 p}{b^2 - a^2}\left(1 + \frac{b^2}{r^2}\right). \tag{46}$$

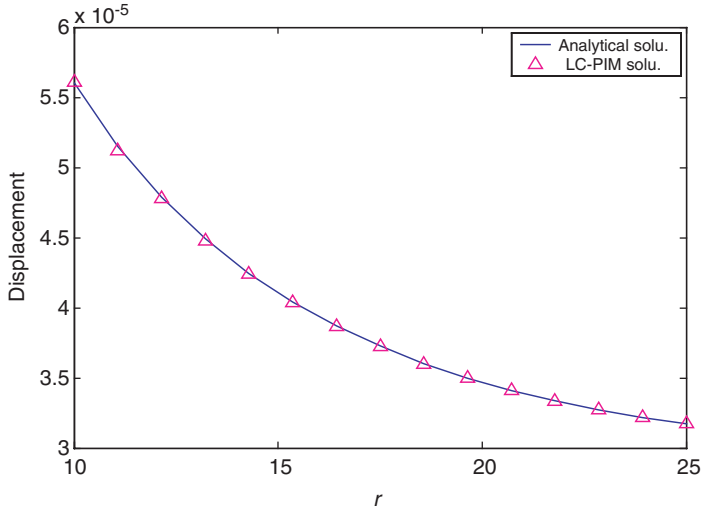

Fig. 13. Displacement distribution along the left edge for the problem of internal pressurized hollow cylinder.

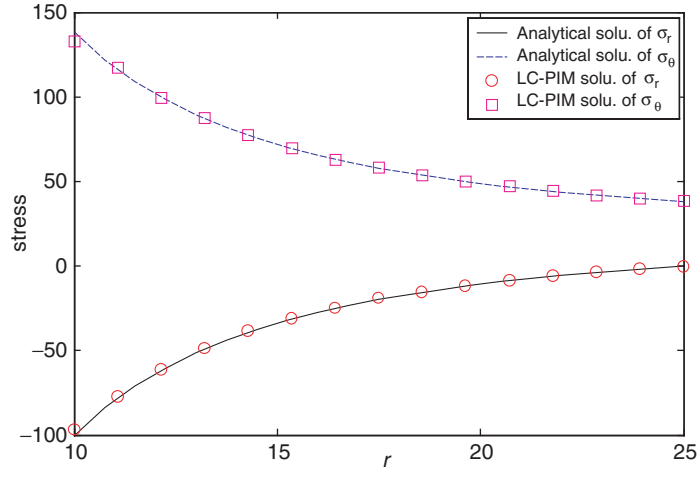

Fig. 14. Stress distribution along the left edge for the problem of internal pressurized hollow cylinder.

In the study, the problem domain is represented with 441 irregularly distributed nodes and the numerical solutions using LC-PIM are plotted in Figs. 13 and 14, together with the analytical solution. It can be observed that both the displacement and stress results are very accurate and stable, and in good agreement with the analytical ones.

3.5. *An automotive part: rim*

Finally, as an application of LC-PIM for practical mechanical components design, a typical rim of automotive component with a complicated shape is studied using the present method. As shown in Fig. 15, the rim is fixed at the nodes around the inner circle and a pressure of 100 units is applied along the lower arc edge of 60°. Displacement and stress results at the nodes along the lower half circle of the rim (marked as dash line ll' in Fig. 15) are computed using the present LC-PIM method. As no analytical solutions are available for this problem, a reference solution is obtained using the FEM software ANSYS, in which a very fine mesh of

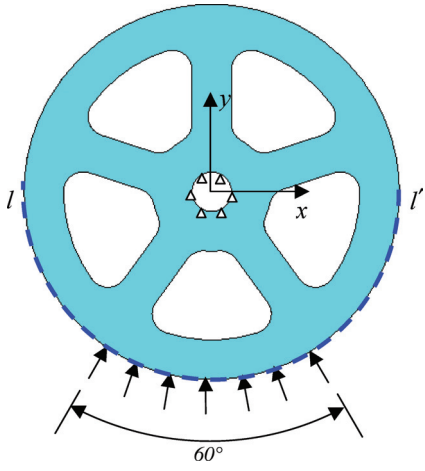

Fig. 15. Model of an automotive rim.

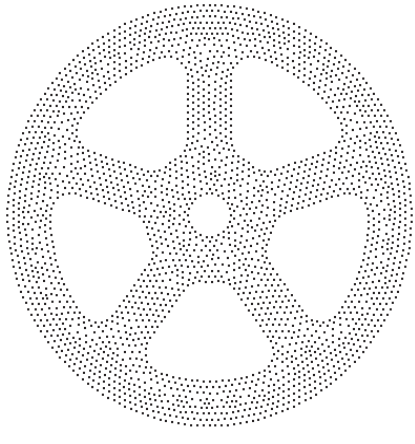

Fig. 16. Node distribution in the automotive rim used for the LC-PIM.

6-node triangle element (18625 elements) is used. The problem domain is represented with 2608 field nodes in our LC-PIM (shown in Fig. 16) and the numerical results obtained using the present method are plotted in Figs. 17–21. It is found that both the computed displacements and stresses are in good agreement with the reference solutions.

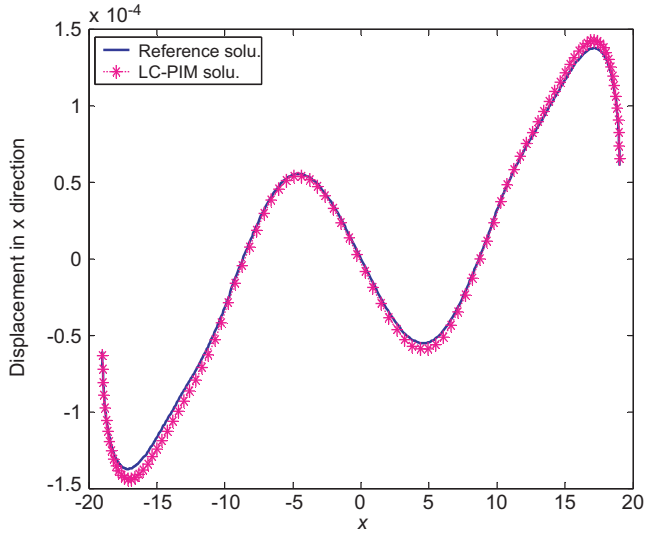

Fig. 17. Distribution of U_x along the line ll' on the boundary of the automotive rim.

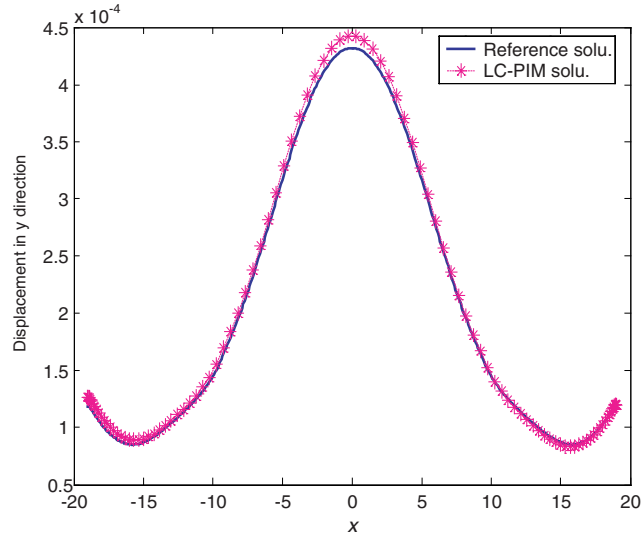

Fig. 18. Distribution of U_y along line ll' on the boundary of the automotive rim.

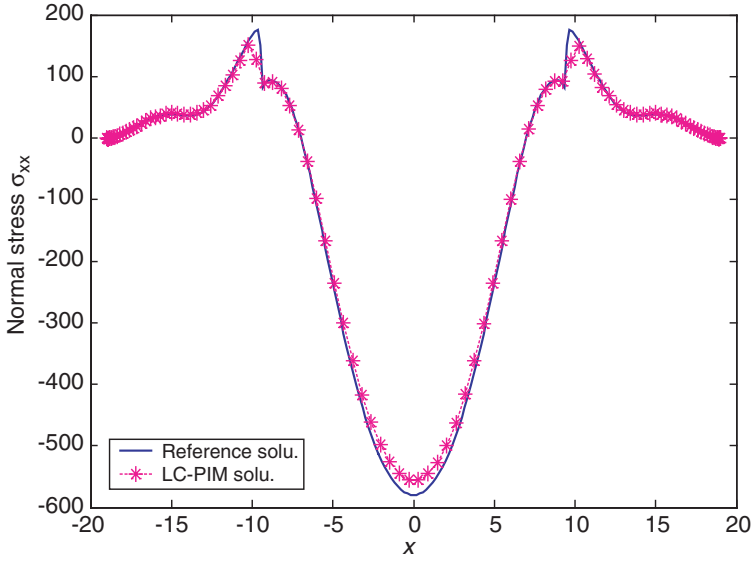

Fig. 19. Distribution of σ_{xx} along the line ll' on the boundary of the automotive rim.

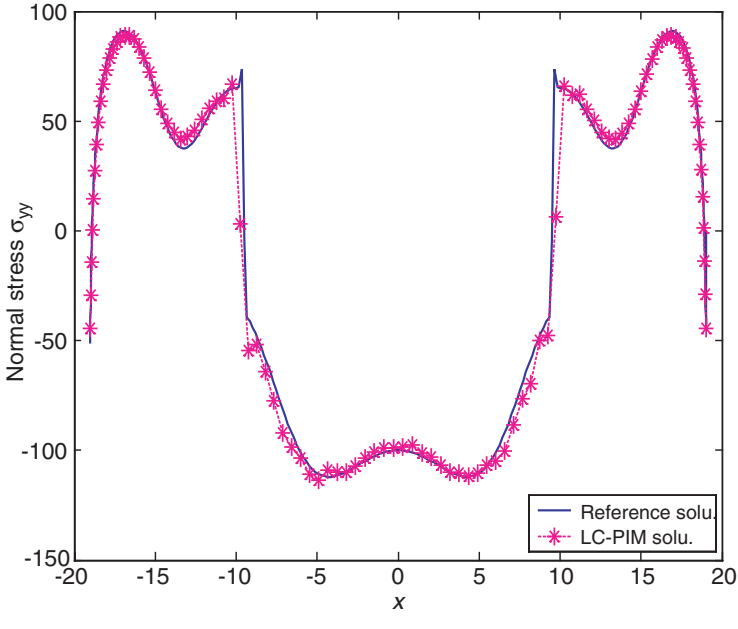

Fig. 20. Distribution of σ_{yy} along the line ll' on the boundary of the automotive rim.

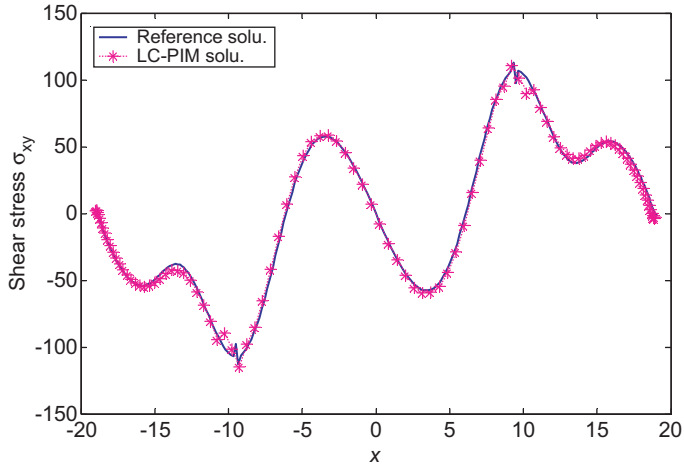

Fig. 21. Distribution of σ_{xy} along the line ll' on the boundary of the automotive rim.

4. Conclusions

In this work, a linearly conforming point interpolation method (LC-PIM) is presented. The method employs polynomial basis functions for field approximation. Galerkin weak form is adopted, and a nodal integration scheme with strain smoothing operation is used. Numerical examples of standard patch test, three benchmark problems, and an actual application problem of a rim with complicated shape are studied using the present LC-PIM method. Very accurate and stable results in terms of both displacements and stresses are obtained and compared with the analytical or reference solutions. From the research, the following remarks can be made.

- Following the present scheme for local supporting nodes selection, the singularity problem of moment matrix in creating the PIM shape functions can be successfully resolved.
- The PIM shape functions generated posses many properties that are also found in the conventional FEM (for example, the Kronecker delta function property) and most numerical techniques and treatments developed in FEM can be utilized with minor modifications.
- Nodal integration scheme with strain smoothing operation is adopted for the numerical integration of the weak form. The present method so constructed guarantees a linear exactness of the numerical solutions, which was also proven numerically by the standard patch test.
- Compared with linear FEM of the linear triangle element, the LC-PIM using exactly the same nodes distribution can achieve a better accuracy and higher convergence rate.

- Compared with the original RPIM based on domain Gauss integration, the present LC-PIM needs no parameters, has higher convergence rate, comparable accuracy, and much better efficiency in the implementation.

As the present method successfully overcomes singularity problem of the moment matrix, ensures linear conformability, and significantly improves the efficiency of computing, the LC-PIM is expected to be further develop to deal with more complicated 3D problems with adaptive analysis capability.

References

Atluri, S. N. and Zhu, T. (1998). A new meshless local Petrov-Galerkin (MLPG) approach in computational mechanics. *Comput. Mech.* **22**: 117–127.

Belytschko, T., Lu, Y. Y. and Gu, L. (1994). Element-free Galerkin methods. *Int. J. Numer. Meth. Eng.* **37**: 229–256.

Chen, J. S., Wu, C. T., Yoon, S. and You, Y. (2001). A stabilized conforming nodal integration for Galerkin mesh-free methods. *Int. J. Numer. Meth. Eng.* **50**: 435–466.

Dai, K. Y., Liu, G. R., Han, X. and Li, Y. (2005). Inelastic analysis of 2D solids using a meshfree RPIM based on deformation theory. *Computer Methods in Applied Mechanics and Engineering* (In press).

Liszka, T. and Orkisz, J. (1980). The finite difference methods at arbitrary irregular grids and its applications in applied mechanics. *Comput. & Struct.* **11**: 83–95.

Liu, G. R. (2002). *Meshfree Methods: Moving Beyond the Finite Element Method*. CRC Press, Boca Raton, USA.

Liu, G. R. and Gu, Y. T. (2001a). A point interpolation method for two-dimensional solids. *Int. J. Numer. Meth. Eng.* **50**: 937–951.

Liu, G. R. and Gu, Y. T. (2001b). A local radial point interpolation method (LR-PIM) for free vibration analyses of 2-D solids. *J. Sound Vib.* **246**(1): 29–46.

Liu, G. R. and Gu, Y. T. (2003). A matrix triangularization algorithm for point interpolation method. *Computer Methods in Applied Mechanics and Engineering* **192**(19): 2269–2295.

Liu, G. R. and Gu, Y. T. (2005). *An Introduction to Meshfree Methods and Their Programming*. Springer, Dordrecht, The Netherlands.

Liu, G. R. and Liu, M. B. (2003). *Smoothed Particle Hydrodynamics — A Meshfree Practical Method*. World Scientific, Singapore.

Liu, G. R., Zhang, G. R., Gu, Y. T. and Wang, Y. Y. (2005). A meshfree radial point interpolation method (RPIM) for three-dimensional solids. *Computational Mechanics*, **36**(6): 421–430.

Liu, W. K., Jun, S. and Zhang, Y. F. (1995). Reproducing kernel particle methods. *Int. J. Numer. Methods Eng.* **20**: 1081–1106.

Lucy, L. (1977). A numerical approach to testing the fission hypothesis. *Astron. J.* **82**: 1013–1024.

Nayroles, B., Touzot, G. and Villon, P. (1992). Generalizing the finite element method: diffuse approximation and diffuse elements. *Computational Mechanics* **10**: 307–318.

Timoshenko, S. P. and Goodier, J. N. (1970). *Theory of Elasticity* (3rd edition). McGraw-hill, New York.

Wang, J. G. and Liu, G. R. (2002a). A point interpolation meshless method based on radial basis functions. *Int. J. Numer. Meth. Eng.* **54**: 1623–1648.

Wang, J. G. and Liu, G. R. (2002b). On the optimal shape parameters of radial basis functions used for 2-D meshless methods. *Comput. Methods Appl. Mech. Eng.* **191**: 2611–2630.

Wang, J. G., Liu, G. R. and Lin, P. (2002). Numerical analysis of Biot's consolidation process by radial point interpolation method. *Int. J. Solids Struct.* **39**(6): 1557–1573.

Zienkiewicz, O. C. and Taylor, R. L., *The Finite Element Method*. 5th edition. Butterworth Heinemann, Oxford, UK.